**RESEARCH PAPER**

# Numerical investigation of the influence of FSW parameters on the heat and mass transfer of austenitic stainless steels

Yuri C. da Silva[1] · Francisco J. V. Oliveira Júnior[2] · Jorge F. dos Santos[3] · Francisco Marcondes[2] · Cleiton Silva[2]

## Abstract

The friction stir weld (FSW) method was developed in 1991 by The Welding Institute (TWI) and is very useful for manufacturing components with low fusion weldability. The success of this relatively new technique is due, in part, to an appropriate combination of some parameters. In order to understand the influence of the parameters such as rotation speed, axial force, and welding velocity, simulations were carried out using the AISI 304L stainless steel. In this work, the process was considered to be a 3D non-Newtonian fluid and the heat input was calculated from the friction between the tool and the plate and from the plastic deformation. The thermal results were compared with the experimental results from the thermocouple measurements. Furthermore, the material flow was related to the formation of defects observed in the experimental welds. The results of the simulation were able to determine the temperature distribution and heat flow, as well as to predict defects in the welding. The simulated viscosity values enabled the prediction of the parameters most likely to cause the formation of flashes. In addition, the injection of inert particles into the model made it possible to predict the formation of wormholes.

✉ Yuri C. da Silva
  yuri.cruz@ifce.edu.br

  Francisco J. V. Oliveira Júnior
  junior180594@alu.ufc.br

  Jorge F. dos Santos
  jorge.dos.santos@hzg.de

  Francisco Marcondes
  marcondes@ufc.br

  Cleiton Silva
  cleiton@metalmat.ufc.br

1  Department of Teaching, Crateús Campus, Federal Institute of Education, Science and Technology of Ceará - IFCE, Cratéus, CE 63708-260, Brazil

2  Department of Metallurgical and Materials Engineering, Center of Technology, Campus of Pici, Universidade Federal do Ceará - UFC, Fortaleza, CE 60455-760, Brazil

3  Helmholtz-Zentrum Geesthacht GmbH, Institute of Materials Research, Materials Mechanics, Solid State Joining Processes, Geesthacht, 21502, Germany

## 1 Introduction

Since the advent of friction stir welding (FSW) in 1991, which was developed by The Welding Institute (TWI) [1], different materials have been welded successfully by this technique including stainless steels. Initially, the FSW technique was used for low melting point alloys such as aluminum and magnesium. Thomas and Nicholas [2] described the advantages of FSW in aluminum alloys for the transportation industries. However, the development of new materials for the FSW tool has enabled other metals, such as steels, to be welded by the FSW technique. Nandan et al. [3] described the welding of austenitic stainless steel using a tungsten tool and Cho et al. [4] welded ferritic stainless steel using a PCBN tool.

In addition to the material of the tools used, the geometry of the tools have also been studied [5]; different geometries can change the mixture between the materials and even develop new techniques, such as the friction stir process (FSP) and stationary shoulder friction stir lap [6–8]. FSP uses the plastic deformation caused by the tool to promote dynamic recovery and recrystallization, aiming to improve the mechanical and metallurgical properties of the surface of the materials [6]. The latter uses a tool, in which the

shoulder is static and the pin rotates. This technique reduces the welding temperature compared with the conventional FSW, and because most of the heat is generated by the pin this can improve the surface finish [7, 8]. Therefore, the FSW has been a precursor process, in developing new techniques.

FSW has many advantages over fusion welding processes. When compared with arc welding, FSW has a lower peak temperature, which is on average 80% of the melting temperature of some metals and alloys. FSW can also refine the grain of some materials when welded; for example, Sato et al. [9] showed that FSW significantly refined the ferrite and austenite phases through dynamic recrystallization. Due to these and other advantages of the FSW process over the traditional welding processes, various studies have, over the last two decades, simulated these complex phenomena.

Despite the numerous advantages of the FSW, the correct combination of parameters is essential to obtain good results. These parameters are responsible for the heat input and material flow during welding. Low thermal input is known to cause problems in the material mixture, such as voids [10], wormholes, and scalloping. On the other hand, excessive high thermal input causes other types of defects, such as root flow, faying surface, and collapsed nugget. Arbegast [11] studied the influence of FSW parameters on the formation of these defects, classifying them in terms of categories and associating them with parameters such as hot and cold, due to their contribution to the thermal input. According to him, an ideal combination of such parameters that prevents the flow-related defects occur when stick-slip wiping flow takes place and the material flow in front of the pin is exactly balanced with the material flow behind the tool.

These flow-related defects can damage the material properties, decreasing the tensile strength of the weld [12], deteriorate the fatigue lifetime [13, 14], favor corrosion and cause problems such as stress concentration and surface finishing [15].

Observing the various physical phenomena involved and the need to choose the correct parameters to obtain a good weld, simulation appears as an excellent tool to understand and predict problems that could occur during a welding.

The first simulations performed by Frigaard et al. [16] with aluminum considered the heat generated by friction but these authors did not take into account the heat generation by plastic deformation.

The evolution of computational tools has enabled other important phenomena to be simulated. The flow of the material around the tool was proposed by Seidel and Reynolds [17] based on 2D fluid flow. Initially, these authors used the viscosity model proposed by Sellars and Tegar [18] and later on they used the viscosity model modified by Sheppard and Wright [19]; in this model, the viscosity was a function of the temperature and the strain rate.

Ulysse [20] used the viscosity model of Sheppard and Wright [19] to develop a 3D model for friction stir welding. The same approach has been used to investigate the FSW technique in other materials, for example, in the studies developed by Nandan et al. [3] with austenitic steel, by Cho et al. [4] with ferritic steel, by Nandan et al. [21] with a titanium alloy, and by Zhu et al. [22] with welding AA2024-T4.

The significant improvements in the simulation models have also made it possible to predict many defects in the FSW process, which in turn have minimized the number of experimental tests necessary. In this work, the simulations of the AISI 304L are validated through different experimental tests. The validated numerical results were used to forecast the conditions that could give rise to some of the defects frequently found in the FSW of the AISI 304L steel. A parameter was developed to predict flash defects and a new way was used to analyze internal defects due to material flow.

## 2 Materials and experimental data

In this work, seven different welding conditions were simulated with the goal to understand how the axial force, the welding velocity, and the rotational velocity affected the final welded material; the welding conditions are given in Table 1. These combinations of parameters were selected from the study developed by Caetano [23].

**Table 1** Experimental parameters investigated

|        | Axial force (kN) | Weld velocity (mm/s) | Rotational velocity (rpm) |
|--------|------------------|----------------------|---------------------------|
| Test 1 | 35               | 1                    | 450                       |
| Test 2 | 50               | 1                    | 450                       |
| Test 3 | 15               | 1                    | 800                       |
| Test 4 | 20               | 1                    | 800                       |
| Test 5 | 35               | 1                    | 800                       |
| Test 6 | 35               | 1.25                 | 800                       |
| Test 7 | 35               | 1.50                 | 800                       |

**Table 2** Chemical composition of AISI 304L stainless steel (% mass)

| Material | Fe | C | Cr | Mn | Ni | P | Si | S | Mo |
|---|---|---|---|---|---|---|---|---|---|
| 304L | Bal. | 0.026 | 18.5 | 1.21 | 7.94 | 0.029 | 0.32 | < 0.010 | 0.29 |

All welds were performed using AISI 304L stainless steel plates of 200 × 500 × 4 mm and the samples were joined along the 500 mm side at the Helmholtz Zentrum Geesthacht (HZG) Center, Germany. The FSW equipment used to perform the welds was the HZG gantry system with a PCBN tool and argon as the shield gas. The chemical composition of the AISI 304L stainless steel used in this investigation is given in Table 2

The thermal properties of the AISI 304L stainless steel and the tool are in Table 3 and it was constructed using Eq. 1 (density), Eq. 2 (thermal conductivity), and Eq. 3 (specific heat).

$$\rho = 7.97 \cdot 10^3 - 6.01 \cdot 10^{-2} \cdot T - 1.12 \cdot 10^{-3} \cdot T^2 + 6.16 \cdot 10^{-7} \cdot T^3 \tag{1}$$

$$k = 19.36 - 0.02960 \cdot T + +6.525 \cdot 10^{-5} \cdot T^2 - 2.88 \cdot 10^{-8} \cdot T^3 \tag{2}$$

$$C_P = 431.73 + 0.2879 \cdot T - 0.000131237 \cdot T^2 + 3.85 \cdot 10^{-9} \cdot T^3 \tag{3}$$

## 3 Physical model

The main assumptions used in this work are presented here. Due to the heterogeneities at the beginning and end of the weld bead, these regions were not considered in this study. The intermediate section of the weld bead had the same heat input, the same physical properties and cross section throughout. These characteristics indicate a steady state regime [25] throughout the intermediate section of the weld bead; consequently, this study analyzed the FSW considering a steady state regime.

The shoulder was considered to be in contact with the top surface of the workpiece as shown in Fig. 1. During the welding, the pin is forced to penetrate into the workpiece, and to a depth that is sufficient to fully stir the workpiece. However, penetration through the plate is undesirable, as the pin should not weld the plate to the backing bar. Thus, a minimum thickness needs to be considered at the bottom of the hole. In this study, the pin length and the thickness of the plate between the tip of the pin and the backing bar were equal to 3.7 mm and 0.3 mm, respectively. Throughout the welding process, the pressure (that is a function of axial force), the rotation, and the welding velocity are assumed to remain constant.

### 3.1 Governing equations

The material was assumed to be a non-Newtonian, incompressible, and viscoplastic fluid. A partial sticking condition is assumed between the tool and the workpiece and the tilt angle of the tool was equal to zero [3]. The reference coordinates are fixed in the center of the tool and at the top of the workpiece. The continuity equation is given by

$$\frac{\partial u_i}{\partial x_i} = 0; i = 1, ..., 3 \tag{4}$$

**Table 3** Thermal proprieties of the materials [24]

| Material | Temperature (K) | Density (kg/m$^3$) | Thermal conductivity (W/m K) | Specific heat (J/kg K) |
|---|---|---|---|---|
| 304L | 298 | 7868.93 | 15.57 | 505.97 |
| | 400 | 7806.18 | 16.11 | 526.13 |
| | 600 | 7663.80 | 18.86 | 558.05 |
| | 800 | 7520.51 | 22.69 | 580.02 |
| | 1000 | 7405.90 | 26.21 | 592.24 |
| | 1400 | 7380.96 | 26.78 | 588.12 |
| | 1800 | 7825.53 | 9.528 | 547.19 |
| PCBN | 298 | 3450.00 | 100 | 750 |
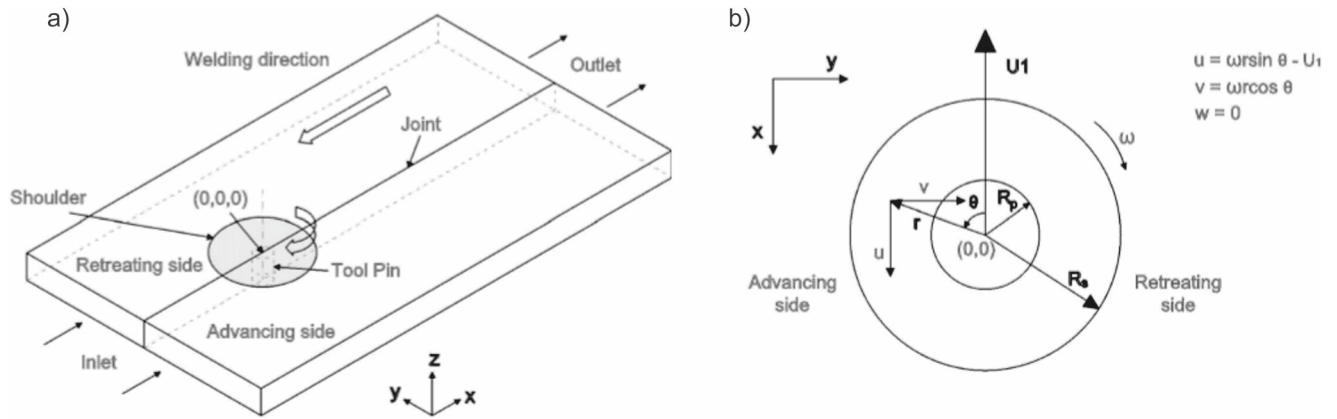
**Fig. 1** Schematic diagram used in the FSW simulation. **a** velocity boundary conditions and **b** view of tool from above

where $u$ is the velocity of plastic flow in $x$-(1), $y$-(2), and $z$-(3) coordinates. Equation 4 states that the volume variation is zero. The momentum conservation equations with reference to a coordinate system attached to the tool using an indicial notation are given by Eq. 5, where $i = 1, 2$ or 3 [4].

$$\frac{\partial \rho u_j}{\partial t} + \frac{\partial \rho u_i u_j}{\partial x_i} = -\frac{\partial P}{\partial x_j} + \frac{\partial}{\partial x_i}\left(\mu \frac{\partial u_j}{\partial x_i}\right) - \rho U \frac{\partial u_j}{\partial x_1} \quad (5)$$

where $U$ is the weld velocity, $\rho$ is the density, $P$ is the pressure and $\mu$ is the non-Newtonian viscosity of the material. The conservation energy equation is given by

$$\frac{\partial(\rho C_P T)}{\partial t} + \frac{\partial(\rho C_P u_i T)}{\partial x_i} = -\rho C_P U_1 \frac{\partial T}{\partial x_1} + \frac{\partial}{\partial x_i}\left(k \frac{\partial T}{\partial x_i}\right) + S_i + S_b \quad (6)$$

The simulations were performed using a steady-state regime. In Eq. 6 $C_P$ is the specific heat and $k$ is the thermal conductivity. $S_i$ is a source term that denotes the rate of energy per unit of volume dissipated by friction between the tool and workpiece, and $S_b$ denotes the rate of energy per unit of volume generated by plastic deformation in the workpiece away from the interface.

## 3.2 Boundary conditions and heat source

The heat source, Si, is added to the commercial software Fluent by means of UDF (user-defined functions) as a heat flux ($q_1$) as described by

$$q_1 = \left[\delta \eta \tau + (1 - \delta)\mu_f P\right](\omega r - U_1 \sin\theta) \quad (7)$$

where $P$ is the pressure of the tool during the welding, $\omega$ is angular velocity, $\delta$ is slip rate, $U_1$ is welding speed,

$\eta$ is the thermal efficiency, $\tau = \sigma_{\text{yield}}/3$ (where $\sigma_{\text{yield}}$ is evaluated using the distortion energy theory for the plane stress) and $\mu_f$ is a friction coefficient. The term ($\omega r - U_1 \sin\theta$) represents the relative velocity between the tool and workpiece. The $\sin\theta$ is defined by

$$\sin\theta = \frac{y}{r} \quad (8)$$

$$\cos\theta = -\frac{x}{r} \quad (9)$$

$$r = \sqrt{x^2 + y^2} \quad (10)$$

where $r$ is the radius with the global axis fixed at the center of the tool.

The source term per unit volume, generated by plastic deformation in the workpiece away from the interface ($S_b$), is defined in Fluent as the heat generation rate in the boundary condition section. This source term is calculated as $f_m \mu \Phi$, where $\mu$ is the viscosity, $f_m$ is an arbitrary constant that indicates the extent of atomic mixing in the system. In this study, a value of 0.04 was used for $f_m$ and the viscous dissipation function $\Phi$ [4] is given by

$$\Phi = 2\left(\left(\frac{\partial u_1}{\partial x_1}\right)^2 + \left(\frac{\partial u_2}{\partial x_2}\right)^2 + \left(\frac{\partial u_3}{\partial x_3}\right)^2\right) + \left(\frac{\partial u_1}{\partial x_2} + \frac{\partial u_2}{\partial x_1}\right)^2 + \left(\frac{\partial u_1}{\partial x_3} + \frac{\partial u_3}{\partial x_1}\right)^2 + \left(\frac{\partial u_3}{\partial x_2} + \frac{\partial u_2}{\partial x_3}\right)^2 \quad (11)$$

The $S_i$ and $S_b$ are split between the tool and workpiece. The fraction inputted into the workpiece ($f$) is defined by [21]

$$f = \frac{J_w}{J_t + J_w} \quad (12)$$

where $J_w$ (workpiece) and $J_t$ (tool) are defined by the following equation:

$$J_i = \sqrt{\left(\rho C_p k\right)_i}; i = w \text{ or } t \tag{13}$$

In Eq. 13, $i = w$ or $t$ for the workpiece and tool, respectively. A convection boundary condition is established for all faces of the plate. For the top of the plate, in addition to the convection heat loss, the thermal radiation is added to the convection flux. After establishing these conditions, the boundary conditions for the bottom, side, and top of the plate are respectively given by the following equations:

$$k\frac{\partial T}{\partial z} = h_b (T - T_e) \tag{14}$$

$$\pm k\frac{\partial T}{\partial y} = h_s (T - T_e) \tag{15}$$

$$-k\frac{\partial T}{\partial y} = h_t (T - T_e) + \sigma \epsilon (T^4 - T_a^4) \tag{16}$$

where $h_b$, $h_s$, and $h_t$ are the coefficient heat convection for bottom, side, and top of the workpiece, respectively; $T_e$ a is the environment temperature; and $k$ is the thermal conductivity.

The velocities in the contact region between tool and workpiece were set in the boundary conditions. For the shoulder, the velocity components are given by

$$v_x = (1 - \delta)(\omega r \sin\theta - U_1) \tag{17}$$

$$v_x = (1 - \delta)(\omega r \cos\theta) \tag{18}$$

For the contact between the tool pin and workpiece, the velocity components are defined by

$$v_x = (1 - \delta)(\omega R_p \sin\theta - U_1) \tag{19}$$

$$v_x = (1 - \delta)(\omega R_p \cos\theta) \tag{20}$$

where $R_p$ is the radius of the pin. All velocity components were implemented in the Fluent simulator using UDF. All experimental parameters such as size of the workpiece, thermal conductivity, and welding speed are shown in Appendix.

### 3.3 AISI 304 stainless steel flow stress

The flow stress for the AISI 304L stainless steel followed a viscosity model based on the simplified Hart's model [26].

In this model the flow stress ($\sigma_e$) is calculated using the sum of $\sigma_p$ (plastic contribution) and $\sigma_v$ (viscous contribution).

$$\sigma_e = \sigma_p + \sigma_v \tag{21}$$

The plastic contribution is the resistance of dislocation entanglement and the viscosity glide. In this model, both plastic and viscosity contributions depend on the temperature and strain rate, and are given by

$$\sigma_p = k_1 \exp\left[-\left(\frac{b}{\dot{\epsilon}}\right)^\lambda\right] \tag{22}$$

$$b = b_0 \left(\frac{k}{G}\right)^N \exp\left[-\left(\frac{Q}{RT}\right)\right] \tag{23}$$

$$\sigma_v = G \left(\frac{\dot{\epsilon}}{a}\right)^{1/M} \tag{24}$$

$$a = a_0 \exp\left[-\left(\frac{Q^0}{RT}\right)\right] \tag{25}$$

where $T$ is the absolute temperature ($K$) and $R$ is the universal gas constant. The other constants are material parameters and they are determined from the experiments. These parameters were determined by Cho et al. [27], who developed a study about the modeling of strain hardening and texture evolution of the 304 stainless steel in FSW. The $k_1$ parameter is the maximum value of viscosity contribution for the stress flow. The saturation value of $k_1$ depends on temperature and strain rate; however in Hart's model it is replaced by Eqs. 26 and 27 [27].

$$k_1 = \left(\frac{C}{\varphi}\right)^{m_0} \tag{26}$$

where the Fisher factor $\varphi$ is given by [28]:

$$\varphi = T.\ln\left(\frac{D_0}{\dot{\epsilon}}\right) \tag{27}$$

Figure 2 shows the viscosity profiles as a function of the strain rate and temperature.

## 4 Results and method

All simulations performed in this work used a non-uniform grid composed of only hexahedron elements that was modeled using the ICEM-Mesh Software. As shown in Fig. 3, local grid refinement was performed in the tool region, since this is the area where the gradients are expected to be higher. Therefore, based on the work of
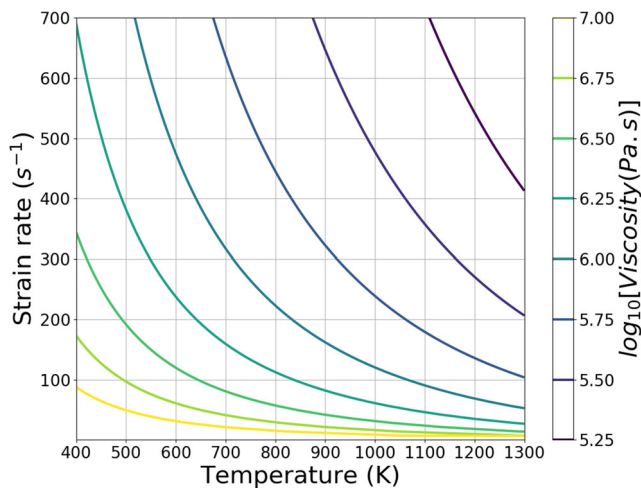
**Fig. 2** Logarithm base 10 of the viscosity (Pa s) profiles for the 304 stainless steel as a function of temperature and strain rate [29]

Silva et al. [29], a grid refinement study with 1,227,002 volumes and 1,296,068 nodes was chosen for all simulations presented in this section.

The numerical results in terms of temperature cycles of this work were compared with the experimental results of Caetano [23], who evaluated the temperature cycles during the welding of AISI 304 stainless by FSW. In the experimental study performed by Caetano [23], six thermocouples were positioned on the top surface of the steel plate, at positions 15, 20, and 25 mm away from the weld centerline; three thermocouples were positioned on the advanced side and the other three were placed on the retraction side of the weld. The weld bead width was equal to 23.6 mm; consequently, the distance from the tool

to thermocouples was 3.2 mm, 8.2 mm, and 13.2 mm, respectively. Figure 4 shows the comparison in terms of the temperature cycles between experimental and simulation results for Test 1. This figure shows that the temperature peaks reached in the simulated results were very close to the peaks determined experimentally, for both sides of the weld bead. Although some minor differences between the numerical and the experimental results were observed, especially those furthest away from the pin, the differences did not exceed 50 K.

After the validation of the numerical approach used in this work, we investigated the effect of different welding conditions presented in Table 1 on the material and weld bead quality.

As shown in Section 3.3, the viscosity depends on the strain rate and temperature. Table 4 presents the maximum temperature and viscosity on the top of the workpiece and stain rate at the same point in order to observe the influence of each combination of parameters of Table 1 on the viscosity. The results showed that the strain rate and temperature have a great influence on the minimum viscosity.

Comparing Test 1 and Test 4 that have approximately the same temperature (only 2.39% difference) but have a large difference in terms of strain rate (approximately 76.58% difference), the variation in viscosity is 42.24%. However, when comparing Test 1 with Test 2 that have the same strain rate and difference in temperature of almost the reverse of the previous case (temperature difference of 16.04%) and strain rate (variation of 1%), the viscosity changes about 43.24%. Although the influence of temperature in the viscosity is larger than the strain rate, the effect of both on viscosity cannot be neglected.
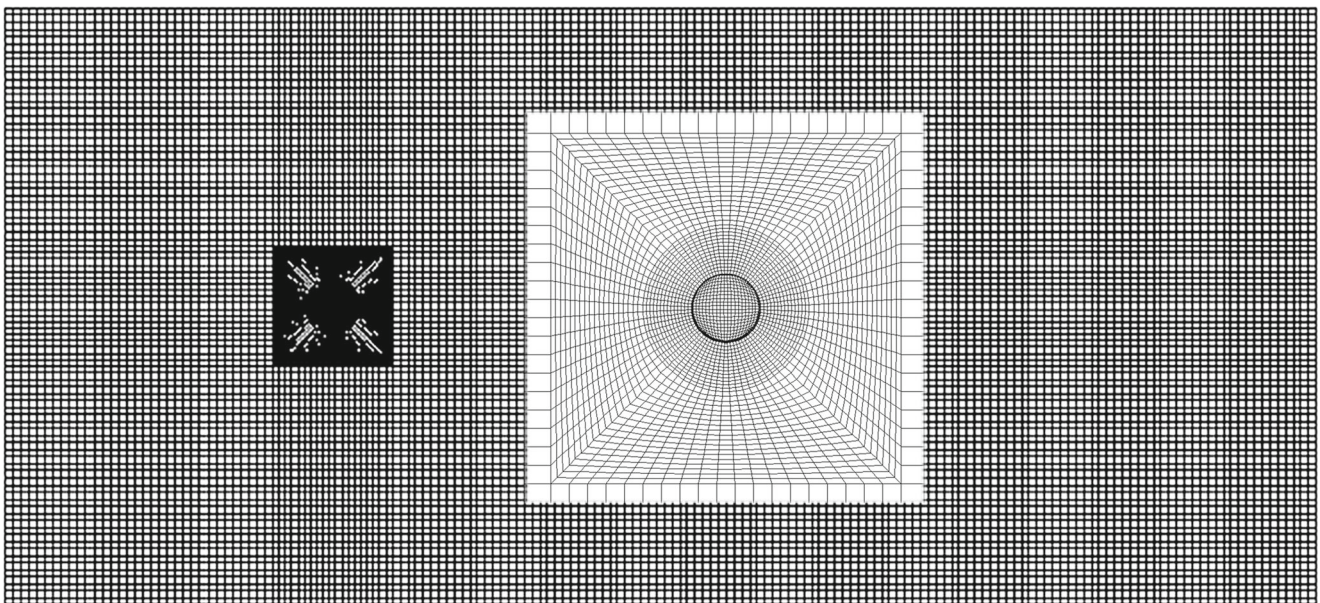


**Fig. 3** Hexahedron grid with 1,227,002 volumes and 1,296,068 nodes used for all simulations
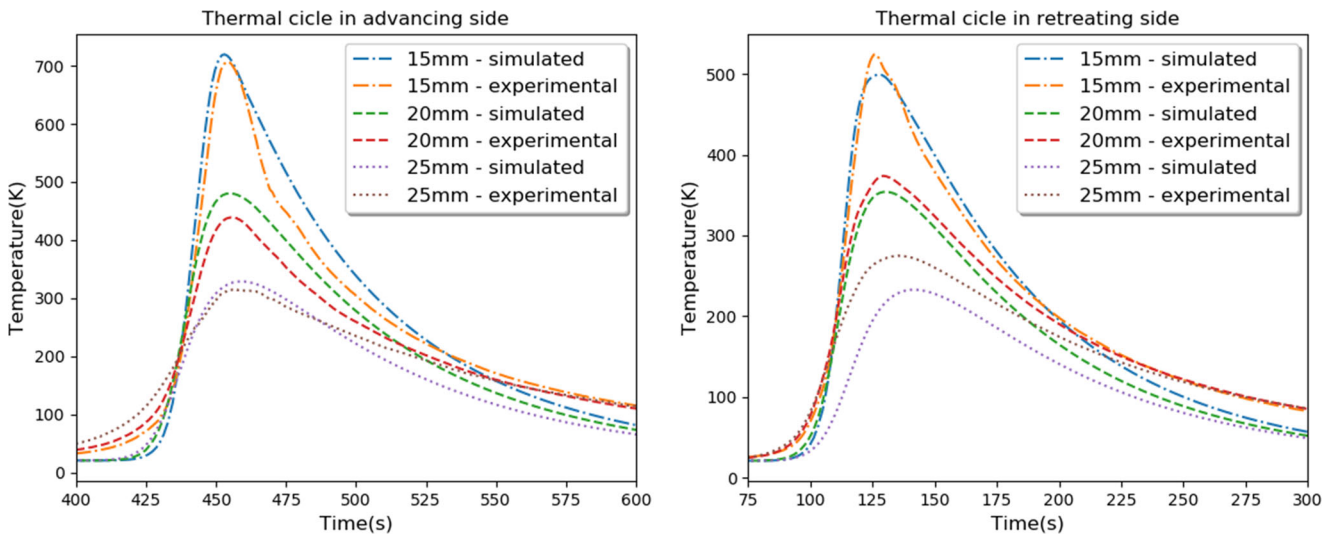
**Fig. 4** Comparison between thermocouples and simulation in different positions along the welding line

Table 4 shows that some tests reached temperatures above or close to the melting point of the steel. These overheated regions occur in thin layers, especially those close to the contact surface with the tool because the simulation does not predict the loss of mass caused by excessive axial force or intense plasticizing. In addition, the friction coefficient used in the current model is constant. Consequently, extreme temperatures should be carefully analyzed because previous studies have shown that in extreme conditions the maximum temperature should be artificially defined [30]. However, in practice, those regions in which the simulation predicted temperatures as high as the melting point would reach a visco-elastoplastic state capable of allowing the material to escape from the nugget in the form of flashes.

The physical model applied in this work has been successfully used to predict the temperature distribution for the group of parameters in which there was a low heat generation or low tendency for flash production, as shown in Fig. 4. However, when this model is applied to a set of parameters that resulted in high heat generation, it fails to predict a reasonable temperature. Depending on the combination of high rotation speed, high intensity of axial force, or low welding velocity, the heat generated is too high, indicating that the temperatures are too high for practical purposes.

Therefore, in this later case, where it failed to predict the temperature field correctly in the contact region between the workpiece and the pin, because it did not consider that the plasticized material will be forced to flow out of the nugget. However, it physically expected that the material in the regions mentioned above is expelled in a solid-state before reaching the extremely high temperatures. Some aspects of these problems are commented on in the text of this section.

Figure 5 presents the temperature distribution at the center of the pin for all welding conditions presented in Table 1. The results clearly verified that the heat generated for high rotation, axial force, and low weld velocity will contribute to a temperature above the melting point close to the contact surface.

**Table 4** Investigation into the effect of the temperature and stain rate on the viscosity

| Test | Maximum temperature | Maximum strain rate | Minimum viscosity |
|------|---------------------|---------------------|-------------------|
| 1 | 1383.87 K | 235.12 s$^{-1}$ | $1.85 \cdot 10^4$ kg/m s |
| 2 | 1606.05* K | 249.24 s$^{-1}$ | $1.07 \cdot 10^4$ kg/m s |
| 3 | 1325.33 K | 425.99 s$^{-1}$ | $1.47 \cdot 10^4$ kg/m s |
| 4 | 1426.57 K | 428.65 s$^{-1}$ | $1.08 \cdot 10^4$ kg/m s |
| 5 | 1875.66* K | 471.97 s$^{-1}$ | $0.46 \cdot 10^4$ kg/m s |
| 6 | 1777.18* K | 474.49 s$^{-1}$ | $0.47 \cdot 10^4$ kg/m s |
| 7 | 1733.79* K | 477.13 s$^{-1}$ | $0.40 \cdot 10^4$ kg/m s |

*The higher temperatures do not occur in practice, they occur due to the method limitations, as discussed in the text
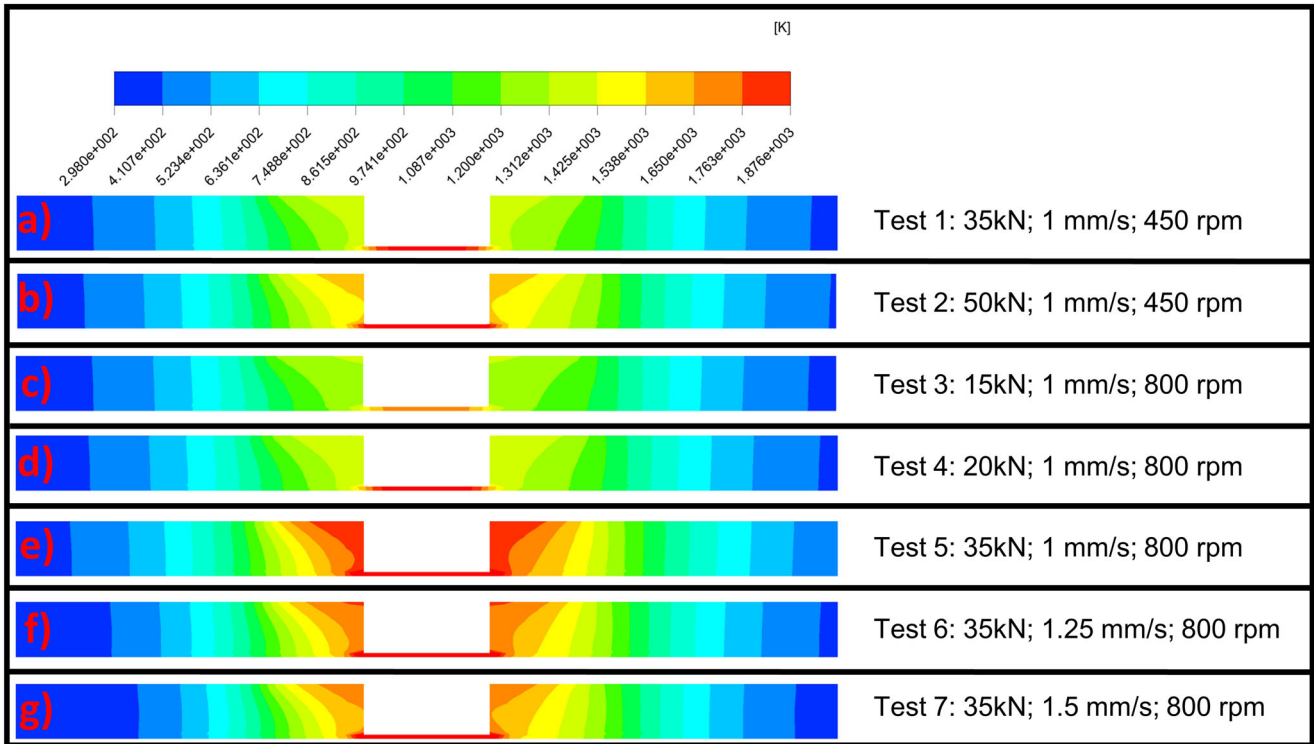
**Fig. 5** Temperature cross section at the center of the pin. **a** Test 1, **b** Test 2, **c** Test 3, **d** Test 4, **e** Test 5, **f** Test 6, **g** Test 7

As previously mentioned, the model used in this work does not take into account the loss of mass that occurs during the welding under certain conditions. In addition, it does not consider the reduction of the friction coefficient. Thus, the effect of the friction coefficient on the temperature field was evaluated in additional tests. The reduced friction coefficient of test 5 (1 mm/s, 35 kPa and 800 rpm) is shown in Fig. 6. These additional tests were designed to observe how the friction coefficient can influence the maximum temperature reached. Figure 6 shows that the temperature
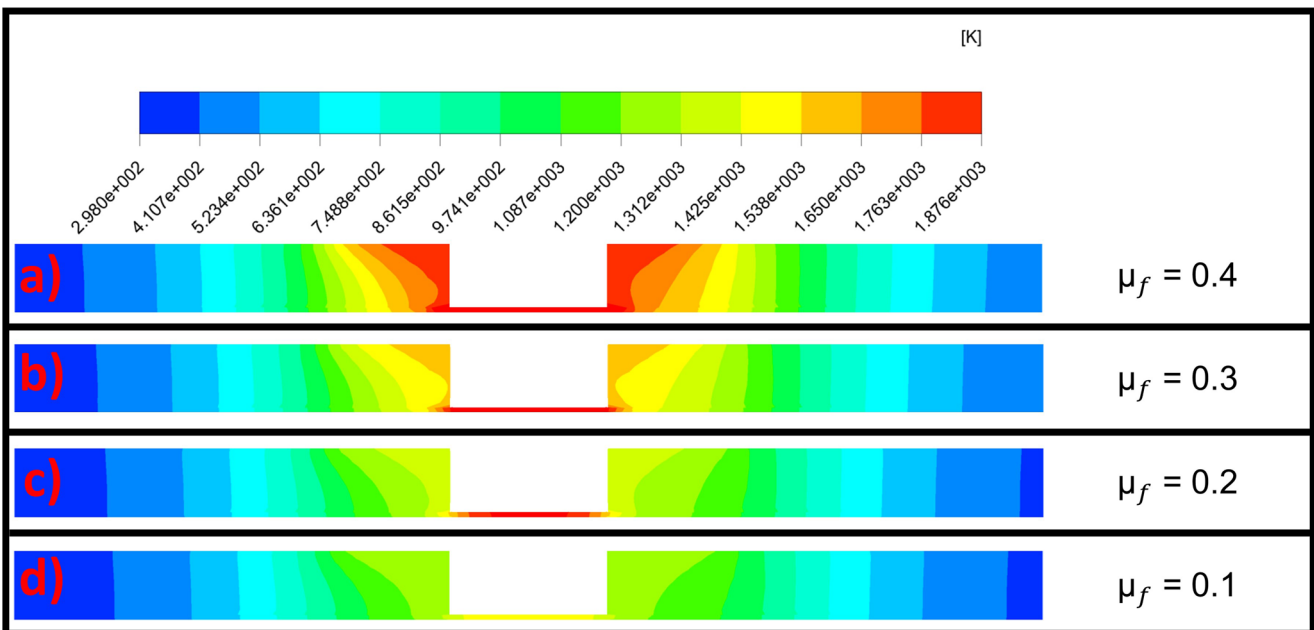


**Fig. 6** Temperature cross section at the center of the pin of Test 5 with different $\mu_f$ values

Fig. 7 Top **a** and transverse **b** sections for Test 5—800 rpm, 1 mm/s and 35 kPa

of the welded region has decreased to levels close to 80% of the melting temperature, as can be seen in Fig. 6c. Su et al. [31] simulated the FSW welding of aluminum alloy under different conditions and their friction coefficient ($\mu_f$) and slip rate ($\delta$) were not constant and changed with the welding conditions. In the present study, there are no experimental results taken from the hotter tests which would permit adjustments and correction in this model; thus ensuring accuracy for the entire range of parameters tested, specifically from the temperature distribution point of view. However, the goal of the above tests is to show that the friction coefficient ($\mu_f$) will have a significant influence on the maximum temperature reached, and that future studies on the FSW process of stainless steel are still necessary to develop functions for variable friction and slip rate coefficients.

The high temperatures observed in Figs. 5 and 6 are due to the contribution of different welding parameters and may be related to defects in the weld. Figure 5, with lower rotation, shows that when the axial force is increased from 35 to 50 kN (Tests 1 and 2), the temperature does not rise as much as was observed for the increase of rotation from 450 to 800 RPM (Tests 1 and 5). This indicates that rotation is the main parameter responsible for the generation of heat. In fact, from the Test 5 results, which was performed applying an axial force of 35 kN and a rotation of 800 rpm, the temperature distribution along the cross section presented some regions that tended to reach extremely high temperatures (Fig. 5e). This result corroborates with the experimental results for this condition that indicated an intense production of flashes and poor surface finish, as shown in Fig. 7.

The above results cannot possible mean that defects such as flashes will only occur when the temperature rises dramatically, as observed in Tests 5 through 7. For instance, for Test 2 that was welded with the highest axial force (50 kN) but using a lower rotation (450 RPM), such high temperatures were not found. Nonetheless, when tested experimentally, this condition showed an excessive flash formation (Fig. 8). These previous results suggest that the combination of low viscosity and high pressure is also very detrimental, contributing to the formation of flashes. Therefore, there is an axial force limit at which the heated material, whose viscosity has decreased due to the contribution of heating, does not have enough strength to withstand the pressure applied by the tool, and therefore is expelled from the weld in the form of flashes.

Since these several tests performed with different welding parameters showed similar behavior concerning the formation of flashes and considering that the main parameters associated with these defects are pressure (axial



Fig. 8 Transverse section for Test 2—450 rpm, 1 mm/s and 50 kPa

**Table 5** $Y$ values for all tests

| Test | $Y$ |
|---|---|
| 1 | 87.07 |
| 2 | 213.91 |
| 3 | 26.27 |
| 4 | 47.68 |
| 5 | 223.08 |
| 6 | 193.81 |
| 7 | 190.13 |

force) and rotation speed, a new empirical parameter has been proposed. The $Y$ parameter was developed to correlate the tendency to form flashes on FSW welds, considering the two main welding parameters responsible for the heating and stirring, as stated in Eq. 28. According to this parameter, the higher the $Y$ value, the greater the tendency to form flashes during welding.

$$Y = \frac{P}{\omega.\mu_{minimum}} \tag{28}$$

where $P$ is the axial pressure calculated from the experimental tool area. Table 5 shows all the $Y$ values for the tests performed.

There is a gradual increase in the $Y$ parameter for the rotation and pressure change for Tests 3 (15 kN and 800 rpm), 4 (20 kN and 800 rpm) and 1 (35 kN and 450 rpm). Therefore, there is a tendency to generate flash when the $Y$ parameter increases. An example of this tendency can be observed in Fig. 9. However, the $Y$ parameter cannot predict other welding problems such as wormholes, as can

be seen in Fig. 9a for Test 3. The wormholes are discussed next.

The wormholes were analyzed using a discrete phase simulation. Inert particles were injected into the fluid and their paths on the plate were recorded. The results of this investigation were plotted in terms of the density plane of the particles after they passed over the tool; we associated the density of the particles that crossed the plane with the tendency to form wormholes. Figure 10 shows a general path of particles in the material. In this and the following figures, "inlet plane" denotes the plane where particles enter the material and "outlet plane" denotes the plane after the tool, where it is possible to see the particle density. The using of discrete phases to predict wormholes was used by other authors to forecast the wormholes in other materials using FSW, see for example, Zhu et al. [22] who used this approach to predict the formation of wormholes in an aluminum alloy.

The difference between the real tool geometry and simulated tool geometry changes the wormhole position. However, this change does not prejudice the prediction of wormhole formation. Figure 11 shows the cross section of Test 1. The experimental results confirmed that a small wormhole at the base of the pin existed, as highlighted in Fig. 11a. The wormhole is predicted in the numerical result by the reduction of particle density as verified in Fig. 11b. As mentioned before, there is a difference in the position of the experimental and numerical wormholes due to the difference in shape of the real and simulated tool. In Fig. 11 this difference was evidenced by the red lines (Real format) and the black lines (Simplified format of the simulation).

Figure 12 compares the differences among the Tests 5, 6, and 7, in which the welding speed is changed and other
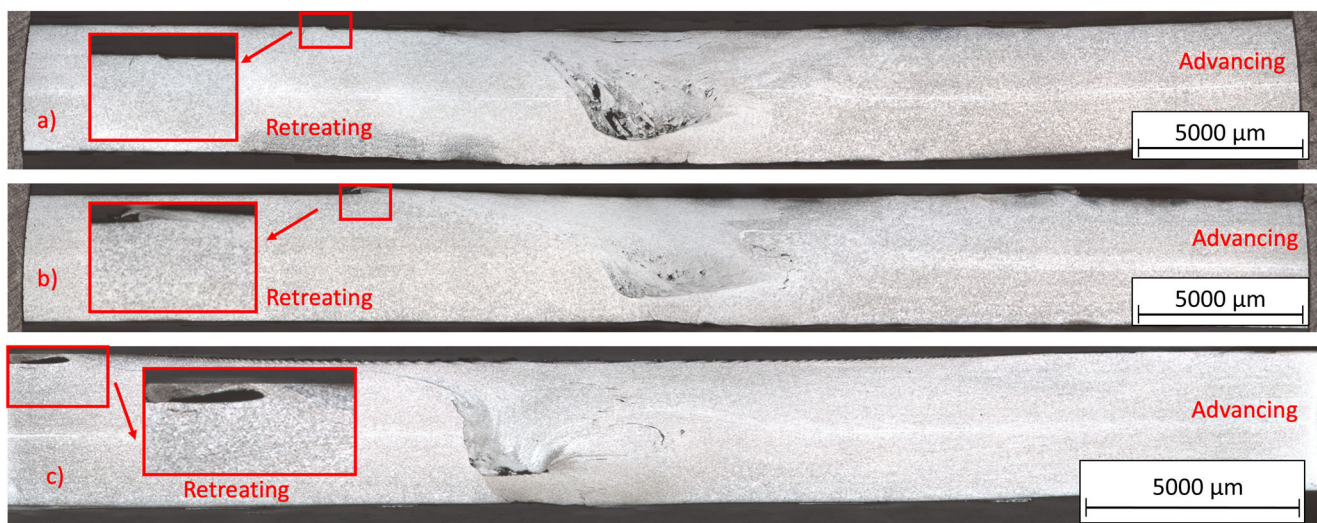


**Fig. 9** Macrography results. **a** Test 3 with $Y = 26.27$, **b** Test 4 with $Y = 47.68$, and **c** Test 1 with $Y = 87.07$
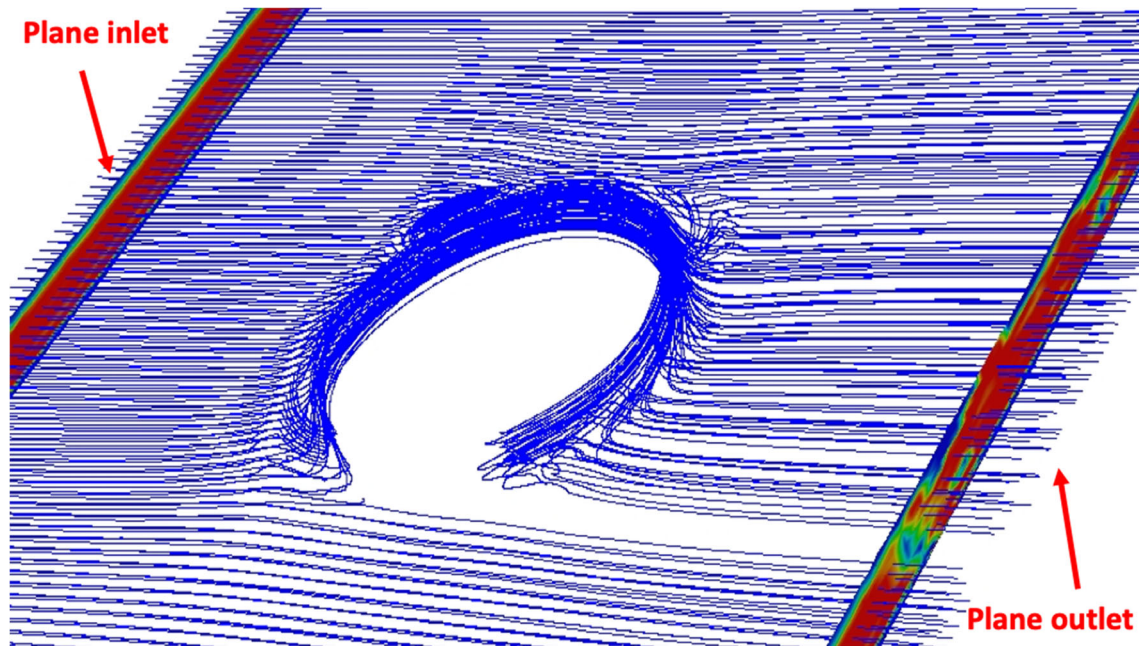
**Fig. 10** The route of the particle(s) in the material

parameters are kept constant. Test 6 verifies that a small wormhole is formed in the simulation results (see Fig. 12d), which is compatible with the experimental result that shows the wormhole in the highlighted region (see Fig. 12c). Test 7 also shows the formation of wormholes in the same region as the simulation. However, the simulation indicated a large area of low particle density throughout the plane when compared with the simulated results of Test 6. This

achievement is once again collaborated by the experimental result (Fig. 12e) that presents a large wormhole in the same location. The experimental test 5 (Fig. 12a) did not have any wormholes; however, the simulation has a lower particle density when compared with Tests 6 and 7. This occurred because this experimental test had other mechanisms of mass loss, such as the flashes previously analyzed.
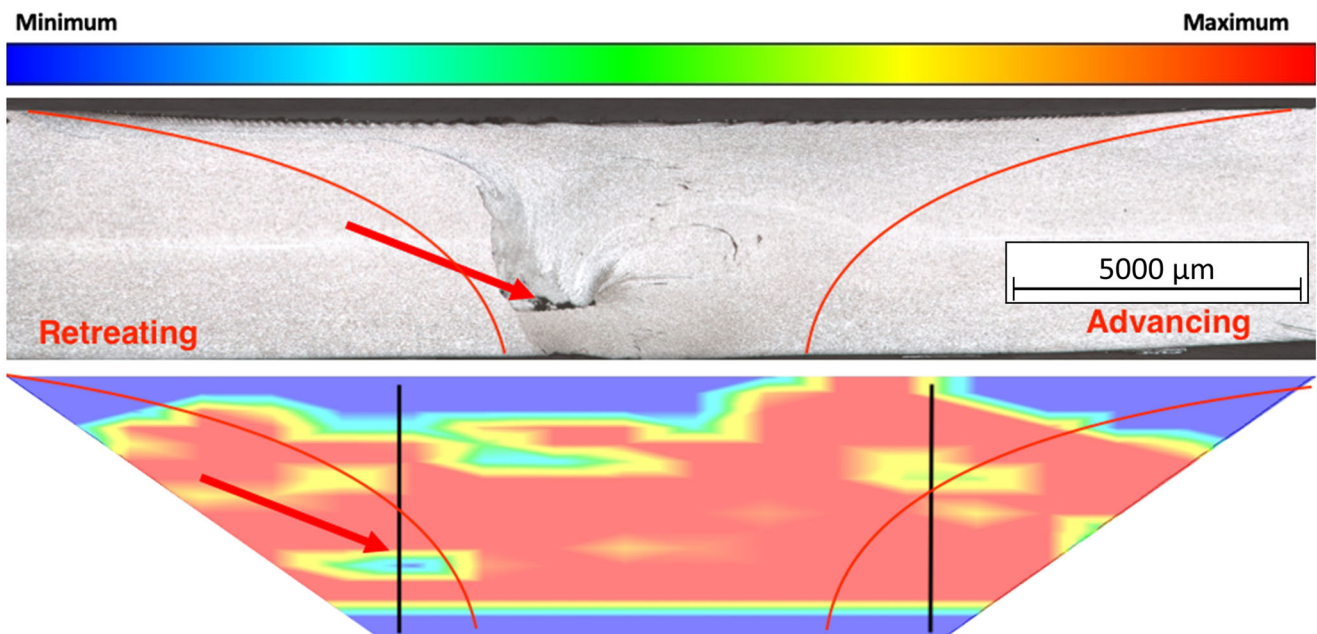


**Fig. 11** Concentration of particles in the plane of Test 1
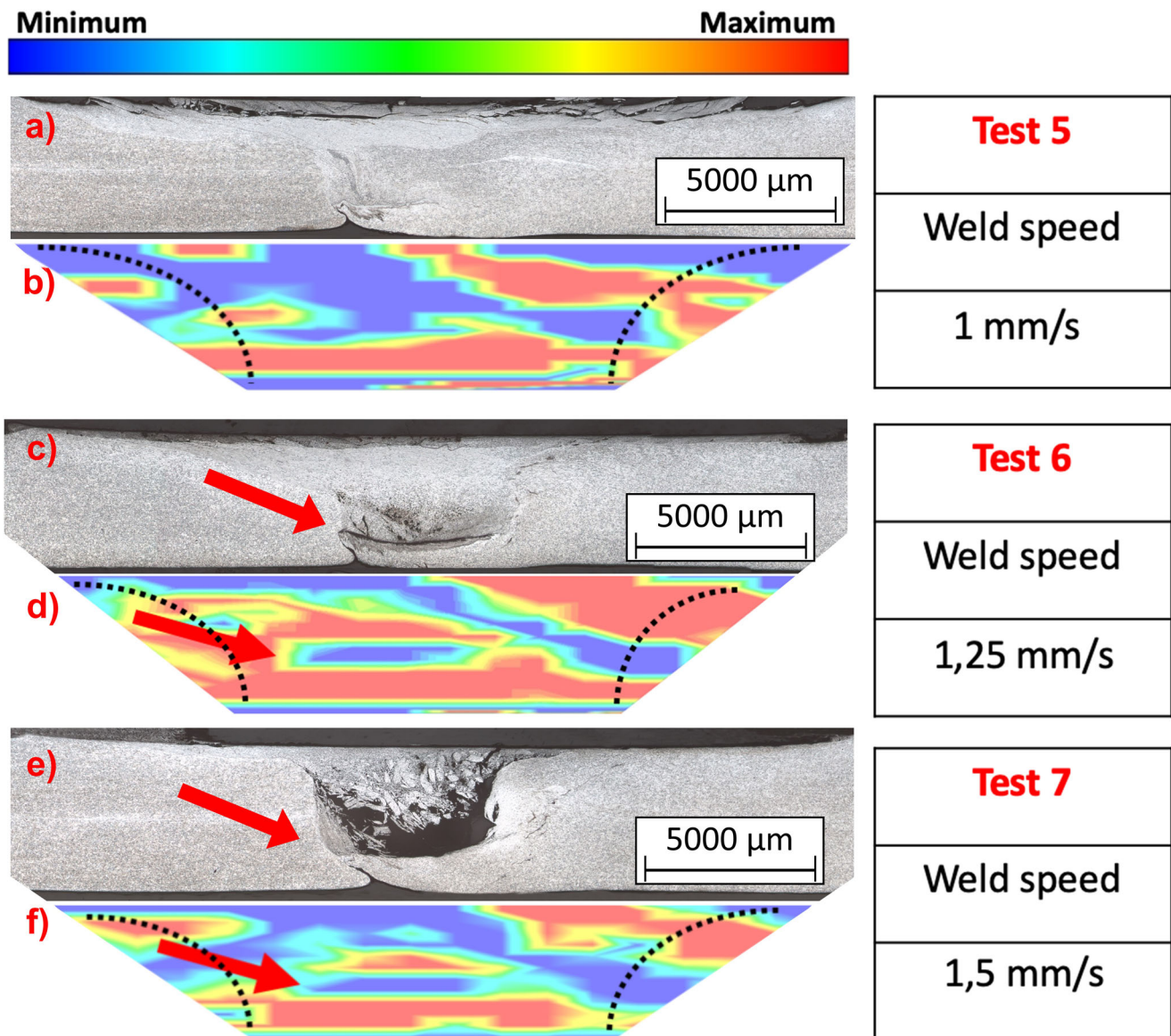
Fig. 12 Experimental and simulated wormholes. **a** Test 5—experimental, **b** Test 5—numerical, **c** Test 6 – experimental, **d** Test 6—numerical, **e** Test 7—experimental, and **f** Test 7—numerical

## 5 Conclusions

In this work, we performed a numerical investigation of FSW for the AISI 304L stainless steel using the commercial simulator ANSYS-Fluent. The numerical thermal cycles were in good agreement with the experimental thermal cycles of the test analyzed; the maximum difference observed between the experimental and numerical thermal cycles was about 50 K for the conditions simulated. We also investigated the effect of several parameters, such as, the axial force, the welding speed, and the rotation on the FSW

process for the AISI 304L stainless steel. The numerical analyzes were able to predict two important defects commonly found in the FSW process: the flashes and the wormholes. In order to investigate the flashes, we proposed the use of parameter $Y$, which depends on the minimum viscosity, the axial force, and the deformation rate. We verified that the flashes increased when the parameter $Y$ increased and this was directly connected to the axial forces. In addition, the discrete phase simulation was an efficient technique to predict wormholes and the welding speed is one of the main factors in the formation of wormholes.

# Appendix . Constants

| $P_N$ (MPa) | (Axial force)$/\pi \cdot R_S$ |
|---|---|
| $R_s$ (mm) | 11.8 |
| $R_p$ (mm) | 4.6 |
| $\eta$ | 0.5 |
| $\delta$ | 0.7 |
| $\mu$ | 0.4 |
| $a_0$ (s$^{-1}$) | $1.36 \cdot 10^{35}$ |
| $b_0$ (s$^{-1}$) | $8.03 \cdot 10^{26}$ |
| $G$ (Pa) | $73.1 \cdot 10^{9}$ |
| $k_0$ (Pa) | $150 \cdot 10^{6}$ |
| $Q$ (J/mol) | $410 \cdot 10^{3}$ |
| $Q_0$ (J/mol) | $91 \cdot 10^{3}$ |
| $\lambda$ | 0.15 |
| $M$ | 7.8 |
| $N$ | 5 |
| $C$ (Pa) | $132 \cdot 10^{6}$ |
| $D_0$ (s$^{-1}$) | $10^{8}$ |
| $m_0$ | 2.148 |
| $n_0$ | 6 |
| $h_b$ (W/m$^2$ K) | 200 |
| $h_s$ (W/m$^2$ K) | 30 |
| $h_t$ (W/m$^2$ K) | 30 |
| $\epsilon$ | 0.3 |
| $A$ (mm$^2$) | 463.55 |

# References

1. Wayne M, Thomas WM, Norris IM, Nicholas ED, Needham JC, Murch MG, Temple-Smith P, Dawes CJ (1991) Friction stir welding process developments and variant techniques, 1991. Patent Application no 397 PCT/GB92/02203 and GB Patent Application no. 9125978.9

2. Thomas WM, Nicholas ED (1997) Friction stir welding for the transportation industries. Materials & Design 18(4):269–273. ISSN 0261-3069. https://doi.org/10.1016/S0261-3069(97)00062-9

3. Nandan R, Roy GG, Debroy T (2006) Numerical simulation of three-dimensional heat transfer and plastic flow during friction stir welding. Metallurgical and Materials Transactions 37A(4):1247–1259. ISSN 1073-5623. https://doi.org/10.1007/s11661-006-1076-9

4. Cho HH, Hong ST, Roh JH, Choi HS, Kang SH, Steel RJ, Han HN (2013) Three-dimensional numerical and experimental investigation on friction stir welding processes of ferritic stainless steel. Acta Materialia 61(7):2649–2661. ISSN 13596454. https://doi.org/10.1016/j.actamat.2013.01.045

5. Kim SD, Yoon JY, Na SJ (2017) A study on the characteristics of FSW tool shapes based on CFD analysis. Welding in the World 61(5):915–926. ISSN 00432288. https://doi.org/10.1007/s40194-017-0478-1

6. Patel V, Li W, Vairis A, Badheka V (2019) Recent development in friction stir processing as a solid-state grain refinement technique: microstructural evolution and property enhancement. Critical Reviews in Solid State and Materials Sciences 44(5):378–426. ISSN 15476561. https://doi.org/10.1080/10408436.2018.1490251

7. Wen Q, Li WY, Wang WB, Wang FF, Gao YJ, Patel V (2019) Experimental and numerical investigations of bonding interface behavior in stationary shoulder friction stir lap welding. Journal of Materials Science and Technology 35(1):192–200. ISSN 10050302. https://doi.org/10.1016/j.jmst.2018.09.028

8. Su Y, Li W, Patel V, Vairis A, Wang F (2019) Formability of an AA5083 aluminum alloy T-joint using SSFSW on both corners. Materials and Manufacturing Processes 34(15):1737–1744. ISSN 15322475. https://doi.org/10.1080/10426914.2019.1669799

9. Sato YS, Nelson TW, Sterling CJ, Steel RJ, Pettersson C-O (2005) Microstructure and mechanical properties of friction stir welded saf 2507 super duplex stainless steel. Materials Sci Eng A 397(1):376–384. ISSN 0921-5093. https://doi.org/10.1016/j.msea.2005.02.054

10. Meng X, Huang Y, Cao J, Shen J, dos Santos JF (2021) Recent progress on control strategies for inherent issues in friction stir welding. Progress in Materials Science 115(June 2020). ISSN 00796425. https://doi.org/10.1016/j.pmatsci.2020.100706

11. Arbegast WJ (2008) A flow-partitioned deformation zone model for defect formation during friction stir welding. Scripta Materialia 58(5):372–376. ISSN 13596462. https://doi.org/10.1016/j.scriptamat.2007.10.031

12. Khan NZ, Siddiquee AN, Khan ZA, Shihab SK (2015) Investigations on tunneling and kissing bond defects in FSW joints for dissimilar aluminum alloys. Journal of Alloys and Compounds 648:360–367. ISSN 09258388. https://doi.org/10.1016/j.jallcom.2015.06.246

13. Kainuma S, Katsuki H, Iwai I, Kumagai M (2008) Evaluation of fatigue strength of friction stir butt-welded aluminum alloy joints inclined to applied cyclic stress. Int J Fatigue 30(5):870–876. ISSN 01421123. https://doi.org/10.1016/j.ijfatigue.2007.06.007

14. Zhou C, Yang X, Luan G (2006) Effect of kissing bond on fatigue behavior of friction stir welds on Al 5083 alloy. Journal of Materials Science 41(10):2771–2777. ISSN 00222461. https://doi.org/10.1007/s10853-006-6337-x

15. Zheng Q, Feng X, Shen Y, Huang G, Zhao P (2017) Effect of plunge depth on microstructure and mechanical properties of FSW lap joint between aluminum alloy and nickel-base alloy. Journal of Alloys and Compounds 695:952–961. ISSN 09258388. https://doi.org/10.1016/j.jallcom.2016.10.213

16. Frigaard Ø, Grong Ø, Midling OT (2001) A process model for friction stir welding of age hardening aluminum alloys. Metallurgical and Materials Transactions A 32(5):1189–1200. ISSN 1073-5623. https://doi.org/10.1007/s11661-001-0128-4

17. Seidel TU, Reynolds AP (2003) Two-dimensional friction stir welding process model based on fluid mechanics. Science and Technology of Welding and Joining 8(3):175–183. ISSN 1362-1718. https://doi.org/10.1179/136217103225010952

18. Sellars CM, McG WJ, Tegart (1972) Hot workability. Int Metallurgical Rev 17(1):1–24. ISSN 0367-9020. https://doi.org/10.1179/imtlr.1972.17.1.1

19. Sheppard T, Wright DS (1979) Determination of flow stress: part1 constitutive equation for aluminum alloys at elevated temperatures. Metal Technology June(June):215–223. ISSN 0307-1693. https://doi.org/10.1179/030716979803276264

20. Ulysse P (2002) Three-dimensional modeling of the friction stir-welding process. Int J Machine Tools & Manufacture 42(July):1549–1557. ISSN 0890-6955. https://doi.org/10.1016/S0890-6955(02)00114-1

21. Nandan R, Lienert TJ, DebRoy T (2008) Toward reliable calculations of heat and plastic flow during friction stir welding of Ti-6Al-4V alloy. Int J Materials Res 99(4):434–444. ISSN 1862-5282. https://doi.org/10.3139/146.101655

22. Zhu Y, Chen G, Chen Q, Zhang G, Shi Q (2016) Simulation of material plastic flow driven by non-uniform friction force during friction stir welding and related defect prediction.

Materials & Design 108:400–410. ISSN 0264-1275. https://doi.org/10.1016/j.matdes.2016.06.119

23. Caetano GQ (2016) Soldagem similar de aços inoxidáveis ferríticos e austeniticos pelo processo "friction stir welding" (joining of similar ferritic and austenitic stainless steels by the "friction stir welding" process). Master's thesis, Universidade Federal do ceará, Campus do Pici - Bloco 729 CEP 60.440-554 - Fortaleza - CE, 2

24. Almoussawi M, Smith AJ (2018) Thermo-mechanical effect on poly crystalline boron nitride tool life during friction stir welding (dwell period). Metals and Materials International 24(3):560–575. ISSN 2005-4149. https://doi.org/10.1007/s12540-018-0074-y

25. Song KJ, Dong ZB, Fang K, Zhan XH, Wei YH (2014) Cellular automaton modelling of dynamic recrystallisation microstructure evolution during friction stir welding of titanium alloy. Materials Sci Technol 30(6):700–711. ISSN 0267-0836. https://doi.org/10.1179/1743284713Y.0000000389

26. Hart EW (1976) Constitutive relations for the nonelastic deformation of metals. J Eng Materials Technol 98(3):193. ISSN 00944289. https://doi.org/10.1115/1.3443368

27. Cho JH, Boyce DE, Dawson PR (2005) Modeling strain hardening and texture evolution in friction stir welding of stainless steel. Materials Science and Engineering A 398(1-2):146–163. ISSN 09215093. https://doi.org/10.1016/j.msea.2005.03.002

28. Fisher ES (1966) Temperature dependence of the elastic moduli in alpha uranium single crystals, part iv (298 to 923 K). Journal of Nuclear Materials 18(1):39–54. ISSN 00223115. https://doi.org/10.1016/0022-3115(66)90094-8

29. Silva YC, Oliveira FJV JR, Marcondes F, Silva CC (2020) Analysis of viscosity function models used in friction stir welding. Journal of the Brazilian Society of Mechanical Sciences and Engineering. https://doi.org/10.1007/s40430-020-02504-1

30. Ma ZY, Feng AH, Chen DL, Shen J (2018) Recent advances in friction stir welding/processing of aluminum alloys: microstructural evolution and mechanical properties. Critical Reviews in Solid State and Materials Sciences 43(4):269–333. ISSN 15476561. https://doi.org/10.1080/10408436.2017.1358145

31. Su H, Wu CS, Pittner A, Rethmeier M (2014) Thermal energy generation and distribution in friction stir welding of aluminum alloys. Energy 77:720–731. ISSN 03605442. https://doi.org/10.1016/j.energy.2014.09.045